Soft Matter

PAPER

View Article Online
View Journal

Cite this: DOI: 10.1039/d6sm00195e

Dynamics of emulsion drop impact, spreading and evaporation: the effect of internal phase gelation

Mario Cordova-Gonzalez, [a] Parisa Bazazi *[b] and S. Hossein Hejazi *[a]

The dynamics of drop impact, spreading, and evaporation on solid surfaces are fundamental to many processes, including agricultural spraying, printing, combustion, and coating. While these behaviors are well understood for single phase liquids, less is known about emulsions with complex internal structures. Here, we report an experimental study on the dynamics of water-in-oil emulsion droplets containing either liquid or gelled aqueous phases. The continuous phase is composed of *n*-heptane and Span 80 micelles, while the dispersed phase is a reactive sodium silicate–ammonium bicarbonate solution that undergoes gelation. Internal gelation changes the rheological response of the dispersed phase and therefore modifies dissipation during spreading and drying. During the impact stage, the dynamics are similar for both emulsion types within our experimental resolution, whereas during the subsequent spreading stage, gel-containing emulsions reach smaller wetted areas. Measured maximum spreading factors are broadly consistent with unified inertial–capillary–viscous scaling for water emulsions, while gel emulsions show systematic deviations at higher internal-phase fractions. Bottom-view fluorescence imaging reveals distinct drying patterns: isolated circular deposits for water emulsions and rugged, interconnected structures for gel emulsions. These findings highlight the importance of the internal droplet structure in governing impact and drying dynamics, with implications for a wide range of emulsion-based technologies.

Received 6th March 2026,
Accepted 6th April 2026

DOI: 10.1039/d6sm00195e

rsc.li/soft-matter-journal

1 Introduction

The impact, spreading, and evaporation of liquid drops on solid surfaces play a critical role in many natural and industrial processes, including agricultural spraying, cooling, enhanced oil recovery, combustion, hydrogel formation, drop-by-drop printing, coating, and drug delivery.[1–11] Multiphase liquid drops, such as emulsions, may contain complex internal structures that influence impact dynamics and, consequently, modify spreading and evaporation behavior. Key contributing factors include changes in apparent viscosity, interactions between the dispersed phase and the solid substrate, capillary effects at internal interfaces, and a reduction in the evaporation rate of the continuous phase.[12–15] Additionally, gelation of the internal phase is widely used in drug delivery applications, where a liquid phase transforms into a gel to support the transport and controlled release of pharmaceuticals.[16,17] These systems represent tunable soft materials where internal rheological transitions can be exploited to control droplet behavior on surfaces.

The liquid-to-gel transition of the internal phase, combined with the impact, spreading, and evaporation of emulsion drops, presents new opportunities for material processing applications such as printing, coating, and transport in porous media. Emulsion-based impact studies are especially relevant for non-contact dispensing of solidifying materials onto solid substrates. However, the influence of internal phase gelation on the complete sequence of impact, spreading, and evaporation remains underexplored, largely due to difficulties in controlling gel-phase deposition.

The impact stage governs the initial droplet morphology and wetted area, influenced by parameters such as impact velocity, surface temperature, and fluid properties.[18–20] For instance, emulsions with low dispersed-phase volume fractions and high Weber numbers (the ratio of inertial to surface tension forces) tend to splash, expelling fluid outward.[12] Following impact, the droplet spreads until it reaches a maximum diameter.[21,22] Gelled emulsions may either enhance or suppress spreading, depending on interfacial adsorption and the volume fraction of the internal phase.

Finally, the continuous phase, which is typically a volatile solvent or fuel, evaporates.[23] During this stage, solidified internal droplets may constrain contact line retraction, reduce evaporation rates, or generate patterned deposits.[15] The overall deposition outcome is therefore influenced by the internal

[a] Department of Chemical and Petroleum Engineering, University of Calgary, Calgary, AB T2N 1N4, Canada. E-mail: shhejazi@ucalgary.ca
[b] Department of Petroleum Engineering, Colorado School of Mines, Golden, USA. E-mail: pbazazi@mines.edu

liquid-to-gel transition. A detailed investigation of these dynamics is needed to understand how internal gelation influences each stage and shapes the final deposition outcome.

In this article, we investigate the impact, spreading, and evaporation dynamics of water-in-oil emulsions on solid surfaces. The emulsions are composed of a continuous oil phase (*n*-heptane with Span 80) and a dispersed phase consisting of either deionized water or a reactive mixture of sodium silicate and ammonium bicarbonate. In the former case, the dispersed phase remains liquid; in the latter, it undergoes a sol–gel transition. Recent studies have also examined the pinch-off dynamics of related emulsion systems, showing that internal phase structure and interfacial stresses can influence filament thinning and breakup during deposition.[24] The gelation process leads to physicochemical transformations that affect droplet spreading, evaporation, and final deposit morphology. Understanding the relationship between internal phase transitions and drop deposition is essential for applications that require precise placement of gelled emulsions, where interfacial flow behavior governs the distribution of the deposited material.

2 Experimental

2.1 Materials

We used a sodium silicate solution (10.6 wt% Na_2O and 26.5 wt% SiO_2, Sigma-Aldrich) as the silica gel precursor and an ammonium bicarbonate dried powder as a reactant (ReagentPlus, 99.0%, Sigma-Aldrich CAS 1066-33-7). We employed *n*-heptane (99%, Sigma-Aldrich CAS 142-82-5) as the main organic phase and a non-ionic surfactant Sorbitan monooleate (Span-80, CAS 1338–43-8) as the micellar source.

2.2 Preparation and characterization of aqueous solutions

We prepared a 2.0 wt% sodium silicate solution and ammonium bicarbonate solutions at concentrations of 1.1 wt%, 2.2 wt%, 2.7 wt%, 3.3 wt%, and 4.4 wt%. Equal volumes of the sodium silicate and ammonium bicarbonate solutions were mixed (1 : 1 volume ratio), resulting in the formation of a silica gel *via* a sol–gel reaction through hydrolysis and condensation-polymerization.[25–28] Throughout this manuscript, we refer to this mixture as the reactant solution. The sample containing 4.4 wt% ammonium bicarbonate is the only one that no longer flows shortly after

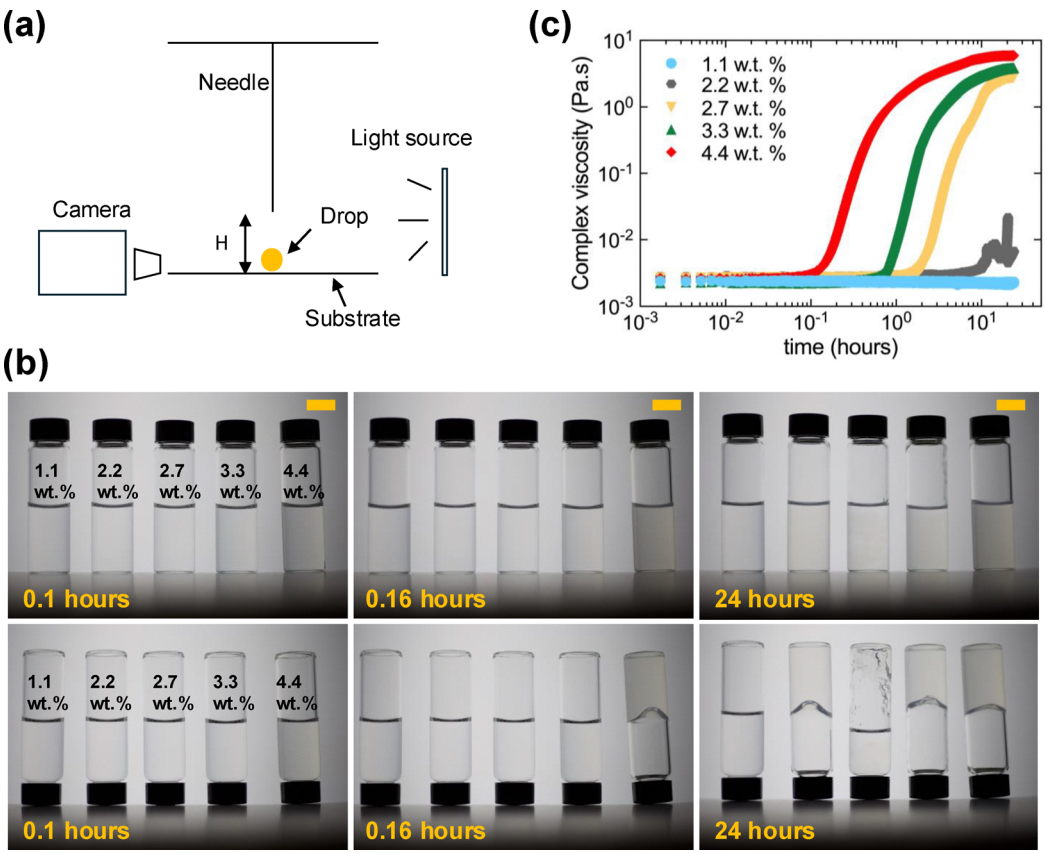

Fig. 1 Schematic illustration of the experimental setup and gel formation process. (a) A glass substrate is placed on a flat surface adjacent to a monochrome camera. Drops are injected at a constant flow rate of 0.2 μL s^{-1} from a height of 30 mm above the glass substrate. The injected volume is 5.6 μL for *n*-heptane and 5.2 μL for all other cases. The drop detaches from the needle, falls under gravity, impacts the solid surface, and spreads. (b) Visual representation of gel formation in samples prepared with 2.0 wt% sodium silicate and 1.1, 2.2, 2.7, 3.3, and 4.4 wt% ammonium bicarbonate, along with corresponding images of inverted bottles. The scale bar represents 1 cm. (c) Oscillation tests performed on all samples shown in (b) at a fixed shear strain of λ = 1.0% and an angular frequency of ω = 10 rad s^{-1}. The onset of gelation is identified by the increase in complex viscosity. Gel formation at 4.4 wt% occurs at 0.16 h and reaches the highest complex viscosity magnitude. All tests were conducted at room temperature (21 °C).

preparation, as shown by the inverted bottle at 0.16 hours in Fig. 1(b), and this concentration is used throughout our study.

We measure the shear rheology of all the samples with a rotational shear rheometer (Discovery Hybrid Rheometer HR 30, TA Instruments) equipped with a concentric cylinder geometry comprising a 30 mm diameter cup and a DIN rotor with an aluminum bob (28 mm diameter and 42 mm length). The sample is loaded within the cup's annular volume (12 mL) and immediately set to the operating gap (2 mm). The temperature is set to 21 °C for all the measurements which is controlled using a Peltier system. To minimize evaporation, we cover the top of the cylinder with two semi-circle plates at a reasonable distance from the rotating bob to avoid direct contact during the tests. First, we conduct a series of continuous oscillation tests in the aqueous mixtures to find out the timing for gel formation and identify the sol–gel transition over 24 hours. The samples are subjected to a controlled shear strain, with constant angular frequency, ω = 10 (rad s^{-1}), and oscillatory strain, λ = 1.0%. We compute the complex viscosity, *i.e.* the complex modulus divided by the applied frequency, as an indicator of how strong and fast the sample is deformed during the oscillation test.[29] Fig. 1(c) shows that samples containing 4.4, 3.3, 2.7, and 2.2 wt% ammonium bicarbonate exhibit initially constant complex viscosities, which begin to increase at approximately 0.16, 1, 2, and 6 h, respectively. This increase indicates the onset of the sol–gel transition associated with the growth and aggregation of silica clusters.[26] Ultimately, the complex viscosity values reach a plateau at about 24 hours. The sample containing 1.1 wt% of ammonium bicarbonate never forms a gel due to the low concentration; instead, colloidal particles of sodium silicate behave as discrete species.[30] Fig. S1 confirms the sol–gel transition times through the crossover of the viscous (G') and elastic (G'') modulus.[29] The gel formation process starts when the elastic behaviour of the solution becomes more dominant. Since the formulation with the combination of 2.0 wt% sodium silicate and 4.4 wt% reactant becomes the most rigid gel within 0.16 h without breaking, it is selected to create the gel emulsions in this study.

2.3 Oil solution preparation

The oil phase, referred to as the micellar solution, consists of 5 wt% Span-80 (Sigma-Aldrich) in *n*-heptane and is used to form water-in-oil (W/O) emulsions.[31–36] The critical micelle concentration (CMC) of Span-80 in *n*-heptane is reported to be approximately 0.018 mM.[37] In this study, we use 5 wt% Span-80, corresponding to a concentration several orders of magnitude above the CMC. At this high concentration, the oil phase contains an abundance of reverse micelles, ensuring that surfactant availability is not limited by bulk depletion. This condition favors rapid coverage of newly created interfaces and enables the formation of aqueous nanodomains[33] capable of hosting reactants, which is essential for the spontaneous emulsification and subsequent gel formation investigated here.

2.4 Emulsion preparation

The emulsification procedure involves adding the aqueous phase, either deionized (DI) water or a freshly prepared reactant solution containing 4.4 wt% ammonium bicarbonate, to the micellar solution. The mixture is then sonicated for 1 minute using an ultrasonic probe at 100% amplitude. Emulsions are stabilized by amphiphilic Span-80 micelles, which entrap aqueous nanodomains containing the sol–gel precursors within their inner cores, facilitating gel formation inside confined microdroplets.[38,39] When the silicate precursor reacts with ammonium bicarbonate, silica polymerization is initiated, leading to the growth and aggregation of silica clusters. This process gradually forms soft, gel-like particles within the dispersed inner phase, while the emulsion remains suspended in a continuous *n*-heptane phase.[15] The onset of gelation, indicated by the rise in G' ($\approx$6 minutes), precedes the G'–G'' crossover ($\approx$9.6 minutes) by approximately 3–4 minutes (Fig. S1a), indicating a short but finite viscoelastic transition regime. Because the emulsification time is significantly shorter than the gelation time, the dispersed aqueous droplets remain fully liquid during emulsion formation.

After sonication, the emulsions are stirred at 250 rpm for 1 h to maintain homogeneity, while the sol–gel transition proceeds to completion. The gel emulsions studied here, therefore, consist of fully gelled aqueous droplets dispersed in oil, rather than suspensions of solid particles formed prior to emulsification. Droplet impact experiments are performed immediately after stirring is stopped (''freshly prepared'' state). From sample loading to completion, the impact measurements require less than one minute; thus, impact experiments are conducted after gelation is complete (gel emulsions) or with a liquid internal phase (water emulsions).The mean dispersed-phase droplet diameter for all emulsion systems is 280 $\pm$ 35 nm, as previously reported.[15] For this study, emulsions are prepared with 5, 10, and 25 vol% aqueous phases.

2.5 Emulsion characterization

We measure the density of the emulsion samples with a portable density meter (DMA 35, Anton Paar) after 1 hour of sample preparation and stirring. The densities are constant and equal to 0.724 $\pm$ 0.05 and 0.720 $\pm$ 0.05 (g mL^{-1}) for water and gel emulsions in the 10 vol% aqueous phase, respectively. Surface tension at the liquid–air interface was measured using a drop shape analyzer (DSA 100, Krüss Instruments). The equilibrium surface tensions of *n*-heptane and the micellar solution were measured to be 20.10 mN m^{-1} and 16.31 mN m^{-1}, respectively. For all water and gel emulsion droplets, the equilibrium surface tension was approximately 16 mN m^{-1}. Finally, we capture fluorescence images of residual emulsion samples, after the evaporation of *n*-heptane, using a confocal laser scanning microscope (Nikon A1R), with 2× and 10× magnification lenses at 1024 × 1024 pixels and 2048 × 2048 pixels, respectively. We deposit drops of water and gel emulsions with a fixed volume of 0.1 μL on a glass slide exposed to air to let the solvent evaporate. We add a fluorescent dye to the oil phase at 0.1 wt% (Kingscote red dye, model 506, 250-R4, Cole-Parmer Canada) and illuminate the drops with a 488 nm (FITC) laser emission at a 10 mW power and with a fixed pinhole of 1.2 AU.

2.6 Drop impact and spreading experiments

The experimental setup consists of a hydrophilic glass slide (VWR, VistaVision) with a known contact angle placed on an automated dosing stage (DSA 100, Krüss Instruments) coupled to a monochrome camera (CF03, Krüss Instruments), as sketched in Fig. 1(a). The camera is perpendicular to the glass substrate with a 2° inclination. The dosing system incorporates a glass syringe and a 0.5 mm diameter stainless steel needle placed 30 mm above the substrate. A drop is formed by injecting at 0.2 μL s^{-1} until the drop detaches from the needle and impacts the glass surface. The injected volume for drop release is kept constant at 5.6 μL for heptane and 5.2 μL for all other liquids, producing drops with initial diameters of D_0 = 2.20 ± 0.05 mm for heptane and D_0 = 2.15 ± 0.05 mm for the remaining tests. The impact velocity in all tests is approximately 0.60 ± 0.05 m s^{-1}, computed from frames immediately before impact. The side-view images of the drop are captured using the camera at 1000 fps and a resolution of 38 pixels per mm. The size of acquired images is 600 × 80 pixels and they are processed using ImageJ to obtain the time evolution of the droplet diameter, $D(t)$.

3 Results and discussion

3.1 Single phase liquids: heptane and micellar solution

We first investigate the impact, spreading, and evaporation dynamics of emulsion-free drops. We then extend this analysis to emulsion-laden drops to examine the influence of dispersed aqueous phases on the overall dynamics. Fig. 2(a) and (b) show the impact, spreading, and evaporation of a drop composed of pure *n*-heptane (surfactant-free) and the micellar solution (surfactant-loaded), respectively. Initially, the drop falls under gravity until it contacts the solid surface. Upon impact, the drop wets an initial area with a diameter denoted as D_i, which we define at t = 1 ms. The drop then rapidly spreads due to the impact, reaching a maximum wetted diameter D_{max}. At this stage, the drop exhibits a toroidal shape with an air cavity at its center, while the outer rim remains continuous. This shape results from capillary waves generated at impact, which propagate along the drop surface.[40,41] The vertical kinetic energy at impact is transferred into radial motion, driving the lateral spread of the drop.[42] As the cavity collapses, the drop edges retract due to the restoring force of the liquid–air interface. The impact behavior is identical for both the *n*-heptane and micellar solution drops, as shown in Fig. 2(a) and (b).

The early-stage spreading is governed by inertial momentum transfer, with a characteristic timescale $\tau_{inert} \sim D_0/U_0$, where $D_0 \approx 2.15$ mm is the initial droplet diameter and $U_0 \approx 0.6$ m s^{-1} is the impact velocity. This yields a timescale on the order of a few milliseconds under our impact conditions. In contrast, surfactant effects require interfacial equilibration, which involves finite adsorption and molecular rearrangement processes, including monomer exchange with micelles and adsorption at the newly created interface. Although the surfactant concentration used here is far above the CMC (≈880 × CMC), implying that bulk depletion is not limiting, interfacial equilibration may still occur on timescales longer than τ_{inert}. Consequently, surfactant-mediated changes in interfacial properties are not expected to influence the very early, inertia-dominated spreading stage, consistent with our observations. After the impact phase, the drop continues to spread and eventually reaches a maximum spreading diameter, $D_{S_{max}}$. The wetting film of the micellar solution drop extends 2 mm farther than that of the surfactant-free drop.

During impact on the glass substrate, a thin liquid film forms as the drop spreads. Because *n*-heptane evaporates rapidly, the film thins quickly and the contact line recedes once the maximum spreading diameter is reached. Surfactant-free droplets retract and evaporate uniformly, leaving no visible residues (Fig. 2(a)). In contrast, droplets containing high concentrations of Span-80 consistently leave sub-millimetric sessile droplets at

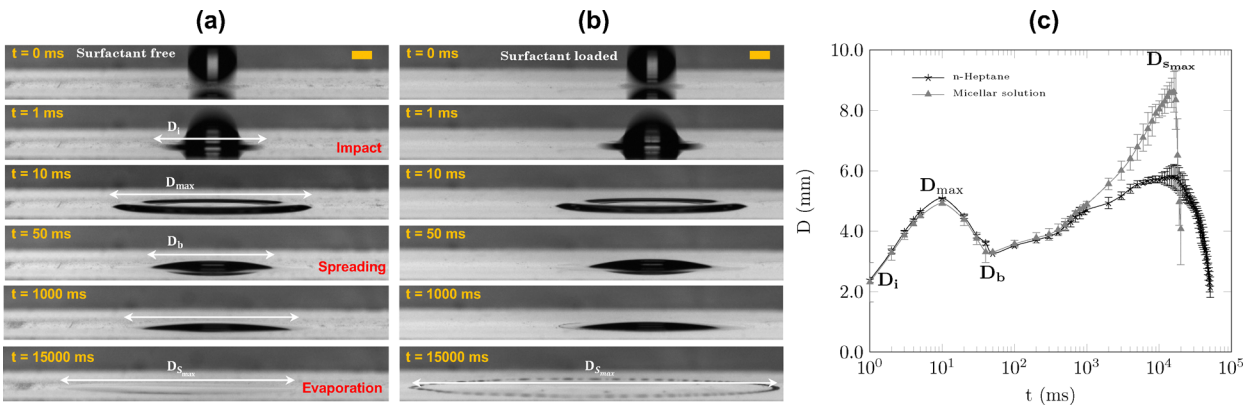

Fig. 2 Impact, spreading, recoil, and evaporation dynamics of (a) a surfactant-free *n*-heptane drop and (b) a surfactant-loaded micellar solution (5 wt% Span-80 in *n*-heptane). Time-resolved images (0–15 000 ms) illustrate the successive stages of impact, spreading, recoil, and evaporation. The initial droplet volume is 5.6 μL for *n*-heptane and 5.2 μL for the micellar solution. The scale bar represents 750 μm. (c) Temporal evolution of the droplet diameter D for *n*-heptane (asterisk markers) and the micellar solution (solid triangular markers). D_i denotes the droplet diameter at initial contact with the substrate; D_b corresponds to the recoiling diameter after maximum spreading; D_{max} is the maximum wetted diameter during the impact stage; and $D_{S_{max}}$ represents the maximum spreading diameter attained during the evaporation stage (t = 15 000 ms). The subsequent decrease in diameter reflects solvent evaporation.

the periphery of the wetted region (Fig. 2b). The formation of these peripheral droplets likely reflects a combination of mechanisms rather than surfactant accumulation alone. Although surface-active molecules migrate toward the interface during spreading and retraction, the adsorption kinetics of Span-80 in a nonpolar solvent are relatively slow, suggesting that classical Marangoni flows may not fully account for the observed deposition. Instead, the rapid evaporation of heptane may induce strong thermal gradients and accelerate film thinning, bringing the liquid layer into a regime where van der Waals forces and disjoining pressure promote rupture. Since both droplets have comparable volumes, the micellar droplet is correspondingly thinner than the heptane droplet and spreads over a larger surface area. This increased interfacial area promotes faster evaporation of the micellar solution compared to the heptane droplet.

3.2 Two phase systems: water-emulsions and gel-emulsions

We next focus on emulsion-laden drops to explore the role of internal phase heterogeneity in shaping drop dynamics. Fig. 3(a)–(c) shows the time sequence of impact, spreading, and evaporation for three cases: emulsion-free, water emulsion, and gel emulsion drops. While the drops adopt similar morphologies during the impact phase, the maximum spreading diameter, $D_{S_{max}}$, is reduced in both water and gel emulsion drops compared to the emulsion-free case. This reduction in $D_{S_{max}}$ is also observed in drops with higher aqueous phase volumes (10 and 25 vol%), as shown in Fig. S2 and S3, respectively.

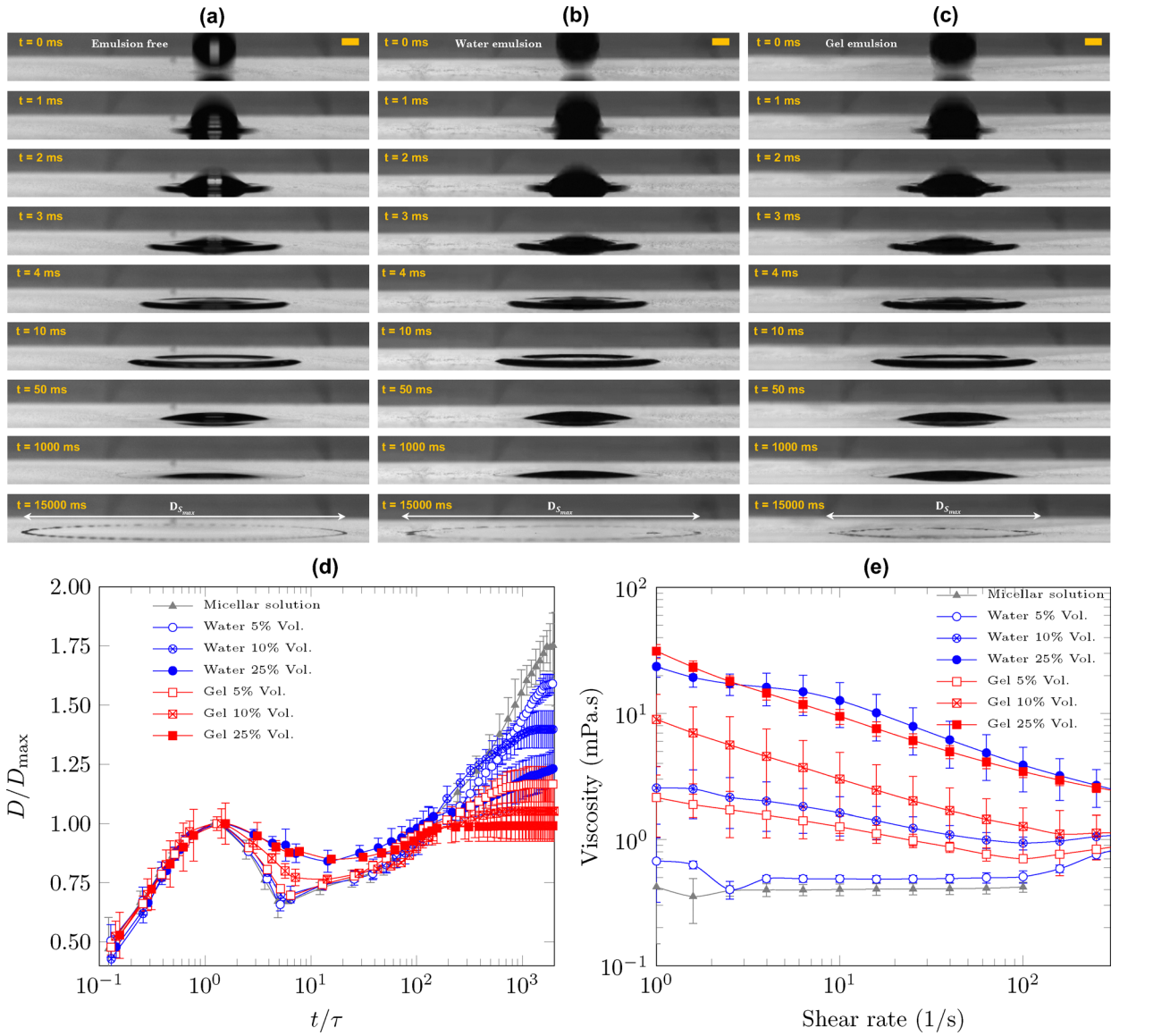

Fig. 3 Impact and spreading dynamics of (a) micellar solution (emulsion-free), (b) water emulsion, and (c) gel emulsion drops in the 5 vol% aqueous phase. The injected volume is 5.2 μL for all drops. The scale bar represents 750 μm. (d) Time evolution of the normalized spreading diameter D/D_{max} as a function of dimensionless time t/τ, where $\tau = D_{max}/U_0$, for micellar solution, water emulsions, and gel emulsions at 5, 10, and 25 vol%. (e) Shear viscosity of micellar solution, water emulsions, and gel emulsions at 5, 10, and 25 vol% as a function of shear rate.

To examine whether the spreading dynamics can be collapsed onto a universal form, we rescale the droplet diameter as D/D_{max} and the time as t/τ, where $\tau = D_{max}/U_0$ is the characteristic inertial spreading time. This normalization has been shown to collapse the spreading dynamics of Newtonian and non-Newtonian droplets over a wide range of conditions.[43] Fig. 3(d) presents the temporal evolution of the scaled drop diameter for the emulsion-free drop (*i.e.*, micellar solution) in gray and for drops with water (blue) and gel emulsions (red) in 5, 10, and 25 vol% aqueous phases. Applying this rescaling to our data (Fig. 3d), we find that the early-time spreading dynamics up to the point of maximum impact area ($D/D_{max} = 1$) collapse for the single-phase liquids as well as for water and gel emulsions across the investigated concentration range.

These results indicate that the proposed rescaling, previously shown to describe inertial spreading in single-phase droplets, remains applicable during the spreading regime of emulsions. In particular, the collapse observed during the spreading phase of impacting droplets (up to $D/D_{max} = 1$) is consistent with the scaling framework introduced by Gordillo *et al.*[44] and further discussed by Gorin *et al.*,[43] in which the spreading dynamics are described by a universal function $D(t)/D_{max} = f(t/\tau)$.

Beyond the point of maximum impact spreading, droplets undergo retraction followed by a slower secondary spreading stage. This late-time evolution depends strongly on composition: for higher aqueous-phase volume fractions (25 vol%), retraction is reduced and the final normalized diameter reaches a lower plateau, with gel emulsions exhibiting systematically smaller D/D_{max} than water emulsions. These deviations reflect additional dissipation associated with the internal microstructure, which is not captured by inertial scaling alone and therefore lies outside the regime of universal collapse.

The maximum spreading diameter, $D_{S_{max}}$, decreases systematically with increasing internal phase volume fraction. A similar trend is observed for the maximum wetted diameter during impact, D_{max}. Previous studies have shown that $D_{S_{max}}$ increases with decreasing contact angle.[45] The apparent contact angle, reported in Table S1, is measured at the first resolvable contact frame prior to significant inertial spreading using ImageJ with the Low Bond Axisymmetric Drop Shape Analysis (LB-ADSA) plugin. After the droplet reaches its maximum spreading diameter, the contact angle decreases below 20°, making reliable quantification difficult; therefore, only early-time contact angles are reported. Emulsion droplets exhibit a slightly higher apparent contact angle compared to the clean liquid droplet, indicating reduced wettability. This suggests that the presence of dispersed internal droplets may hinder early-stage spreading by constraining the advancing contact line. The apparent contact angles are comparable for water-based and gel-based emulsions. In gel emulsions, the stiffer internal droplets may restrict the mobility of the dispersed phase,[46,47] contributing to a further reduction in spreading compared to the more deformable (soft) droplets in water emulsions.

Moreover, we repeated the experiment for a 10 vol% aqueous phase emulsion, with the needle height reduced from 30 mm to 15 mm and 5 mm. The resulting impact velocities were 0.52 and 0.33 ± 0.05 m s^{-1}, respectively, compared to the original 0.60 ± 0.05 m s^{-1}. Fig. S4 shows the collapse of data points up to $D/D_{max} = 1$.

To investigate the role of rheology in spreading and drying behavior, we measured the shear viscosity of micellar solution (emulsion-free), water emulsions, and gel emulsions in 5, 10, and 25 vol% aqueous phases, as shown in Fig. 3(e). To investigate the role of rheology in spreading and drying behavior, we examined the viscosity of water and gel emulsions in 5, 10, and 25 vol% aqueous phases. Fig. 3(e) presents the shear viscosity as a function of shear rate for micellar solution (emulsion-free), water emulsions, and gel emulsions at 5, 10, and 25 vol%. The micellar solution exhibits nearly constant viscosity across a wide shear rate range (approximately 2.5 to 100 s^{-1}), with a slight increase at higher shear rates possibly due to the onset of secondary flow effects. In contrast, both water and gel emulsions display clear shear-thinning behavior. This is observed up to 100 s^{-1} for the 5 and 10 vol% samples and across the full shear rate range for the 25 vol% case. Shear thinning is likely caused by the disruption of inter-droplet interactions or internal gel networks under shear.[48]

The viscosity magnitude increases with higher aqueous phase content, indicating stronger inter-droplet interactions due to reduced spacing between dispersed droplets. Particularly, gel emulsions consistently exhibit higher viscosity than water emulsions at all concentrations tested, which reflects the formation of internal gel structures that resist deformation. These rheological differences contribute directly to the reduced spreading observed in gel emulsions, as the more rigid internal phase offers greater resistance to flow during impact and spreading.

3.3 Dimensionless analysis and scaling of maximum spreading

The impact dynamics are characterized using the Reynolds (Re), Weber (We), and Ohnesorge (Oh) numbers, evaluated from the droplet impact conditions (Table S2). For the present experiments, the characteristic velocity and length scales are taken as the impact velocity $U_0 = 0.6$ m s^{-1} and the initial droplet diameter $D_0 = 2.20 \times 10^{-3}$ m for *n*-heptane and $D_0 = 2.15 \times 10^{-3}$ m for all other cases. The Reynolds number is calculated as $Re = \rho U_0 D_0/\mu$, where ρ is the liquid density and μ is the dynamic viscosity. For emulsions and gel emulsions, which exhibit shear-rate-dependent viscosity, μ is evaluated at a characteristic shear rate associated with impact, approximated as $\dot{\gamma} \sim U_0/D_0 \approx 2.8 \times 10^2$ s^{-1}, based on rheological measurements. The Weber number is computed as $We = \rho U_0^2 D_0/\gamma$, where γ is the liquid surface tension. The Ohnesorge number is then obtained from $Oh = \mu/\sqrt{\rho\gamma D_0}$, which represents the relative importance of viscous effects compared to inertial and capillary forces.

The calculated ranges of dimensionless numbers ($Re \sim 10^2$–10^3, $We \sim 10^1$, and $Oh \sim 10^{-3}$–10^{-2}) place our experiments in the inertial–capillary regime with moderate viscous influence (*i.e.*, low-to-moderate Oh and moderate We), where maximum spreading is governed primarily by the balance between inertia and capillarity. Viscous dissipation becomes increasingly relevant for higher emulsion concentrations as Oh increases. In this regime, recent studies[49] have shown that viscous effects

can influence spreading even at relatively low Oh, consistent with the systematic reduction in spreading factor $\beta_{max} = D_{max}/D_0$ observed as viscosity increases.

We compare the measured maximum spreading factors with both classical empirical scaling laws and a unified inertial–capillary–viscous framework. A commonly used inertial–capillary scaling is $\beta_{max} \sim We^{1/4}$, which neglects viscous dissipation. In addition, we evaluate a smooth-transition ("unified") correlation given by $\beta_{max} \sim Re^{1/5}P^{1/2}/(a_1 + P^{1/2})$, where $P = WeRe^{-2/5}$ and $a_1 \approx 1.24$[43,50,51] (see Fig. 4a). For the single-phase control liquids (*n*-heptane and micellar solution), both scalings predict spreading factors in close agreement with the experiments. The unified model yields $\beta_{max} \approx 2.23$ for heptane and ≈ 2.30 for the micellar solution, compared with measured values of 2.32 and 2.29, respectively. Extending the comparison to emulsion and gel-emulsion droplets using the effective viscosity evaluated at the impact-relevant shear rate shows that the inertial–capillary scaling $\beta_{max} \sim We^{1/4}$ predicts nearly constant spreading across all samples. Because We varies only weakly in our experiments, this scaling cannot capture differences arising from viscosity changes. In contrast, the unified correlation captures the overall trend of decreasing spreading factor with increasing internal phase concentration.

For all water-emulsion samples and the 5 vol% gel emulsion, predicted spreading factors remain in close agreement with the experiments, with deviations typically within a few percent. At higher gel-emulsion concentrations (10 and 25 vol%), however, the unified model overpredicts the measured spreading, indicating that structured internal phases introduce additional dissipation not captured by a single effective viscosity. Plausible contributions include internal microstructural resistance, interfacial deformation, and enhanced contact-line dissipation. At higher gel concentrations, rearrangement of the internal gel droplets during impact may locally increase the effective dispersed-phase volume fraction. Such transient concentration variations could increase dissipation and bring localized regions closer to jammed conditions, thereby reducing spreading.

We further examine the spreading factor D_{max}/D_0 as a function of zero-shear viscosity (Fig. 4b). Although impact occurs at high effective shear rates, μ_0 provides a sensitive measure of microstructural rigidity and network strength, which correlates with additional dissipation mechanisms not captured by a single effective viscosity evaluated at $\dot{\gamma} \sim U_0/D_0$. A monotonic decrease in spreading with increasing zero-shear viscosity is observed. The log–log representation reveals an apparent power-law trend, with distinct slopes for water emulsions and gel emulsions. The steeper slope for gel emulsions suggests additional resistance to spreading arising from the internal microstructure, beyond what is captured by bulk viscosity alone.

An alternative interpretation is to view the gel emulsions as suspensions of soft internal domains dispersed within a liquid continuous phase. In this picture, the gelled aqueous droplets behave as deformable inclusions that may introduce additional dissipation during spreading beyond what is captured by an effective viscosity. Similar considerations arise in the droplet impact of particulate suspensions, where the internal microstructure and particle rearrangements modify spreading and retraction dynamics. Recent work by Shah and Driscoll discusses how suspended phases in complex fluids can influence droplet impact behavior even at moderate volume fractions through shear-thinning effects and microstructural rearrangements.[52] In the present system, the internal gel droplets may play a similar role by resisting deformation and constraining flow within the spreading droplet.

Similar behavior has been reported for droplets containing rigid particle suspensions. Experiments on suspension drops

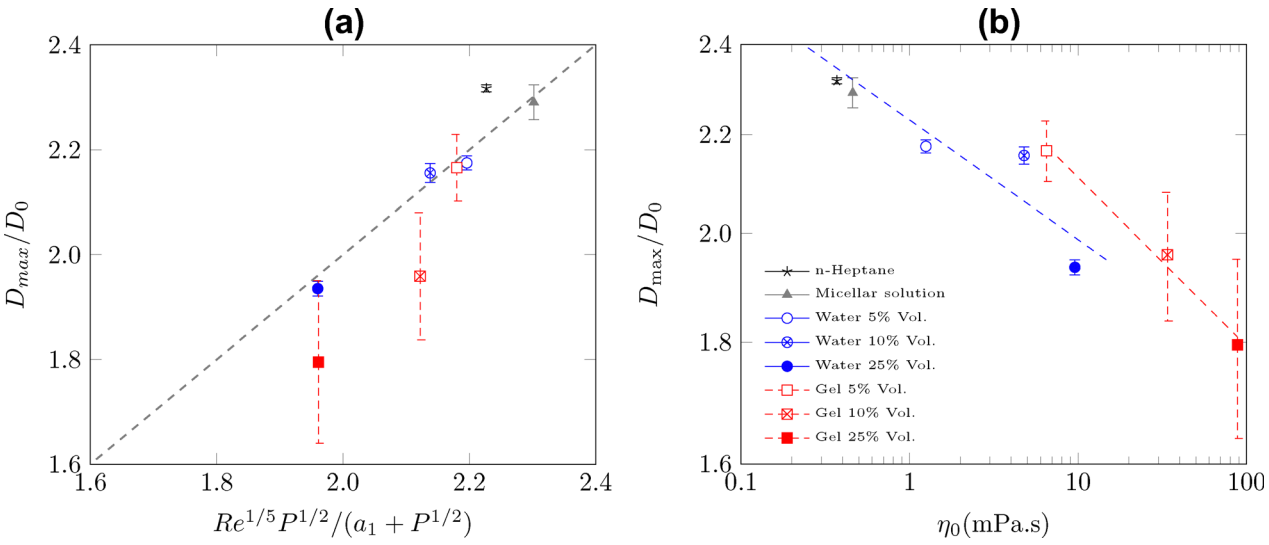

Fig. 4 Maximum spreading factor D_{max}/D_0 as a function of (a) the unified correlation $Re^{1/5}P^{1/2}/(a_1 + P^{1/2})$ and (b) zero-shear viscosity (log–log scale) for heptane, micellar solution, water emulsions, and gel emulsions. The spreading factor decreases systematically with increasing viscosity. Gel emulsions exhibit a steeper power-law decay compared to water emulsions, suggesting additional microstructural resistance to spreading. Error bars represent the standard deviation from at least three independent impact experiments.

show that increasing particle volume fraction generally reduces the maximum spreading factor due to additional dissipation arising from particle rearrangements and particle–fluid interactions during impact.[53,54] At sufficiently high particle concentrations, deviations from classical Newtonian scaling can emerge as particle interactions and microstructural effects influence the impact dynamics.[55] Although the present emulsions contain deformable gel droplets rather than rigid particles, the qualitative trends observed at higher gel concentrations are consistent with the broader behavior reported for suspension droplets.

Nevertheless, the ability of the unified framework to reproduce the overall trend of decreasing β_{max} with increasing Oh suggests that inertia, capillarity, and viscous dissipation remain the dominant controlling mechanisms. The systematic deviations observed at high gel concentrations indicate the need for future extensions of the model to explicitly account for multiphase and structured-drop effects.

3.4 Evaporation of water-emulsions and gel-emulsions

Beyond impact and spreading, evaporation constitutes the final stage of the droplet dynamics under investigation. However, limitations in side-view imaging, such as the rapid evaporation rate and the accumulation of the material near the droplet center, prevent reliable quantification of evaporation dynamics, including contact line recession, in emulsion systems. Therefore, we present bottom-view observations of drop deposition and film dewetting on the glass surface to gain further insights into the evaporation behavior.

Fig. 5(a) and (b) depict bottom-view fluorescence images of drying drops containing either water emulsions (a) or gel emulsions (b) in 5, 10, and 25 vol% aqueous phases. Each column corresponds to a different emulsion volume fraction, and each row represents a different time point during evaporation.

At early times (t = 10 s), the drop footprint is intact across all cases, showing uniform fluorescence from the micellar solution, where Span 80 micelles encapsulate either water or gel. As *n*-heptane begins to evaporate, distinct dewetting patterns emerge. By t = 60 s, water emulsion samples display increasingly heterogeneous structures, with radial fingering and isolated micelle clusters more prominent at higher aqueous fractions. In contrast, gel emulsions show more uniform deposition without pronounced radial features.

At late times (t = 600 s), the continuous *n*-heptane phase has fully evaporated, leaving behind non-volatile Span 80 and the internal aqueous structures. Water emulsions produce dispersed, near-circular deposits that remain mostly isolated. At 25 vol%, the deposits appear larger and more widely spaced, which may result from coalescence during the drying process, from initial differences in emulsion packing and droplet stability, or from partial evaporation of water from the internal phase. Partial water loss from the internal phase may shrink droplets or promote coalescence during drying.

In gel emulsions, however, the final pattern differs significantly. Instead of discrete near-circular deposits, the residual film fragments into irregular, branched, or network-like structures. These features become increasingly coarse and interconnected with higher gel content, indicating that gelation within the internal phase inhibits droplet mobility and promotes structural rigidity during drying.

High-magnification insets in the bottom two rows further confirm the morphological contrast. Water emulsion residues show smooth, spherical features, while gel emulsions leave behind rugged, interconnected deposits. These observations suggest that the rheological properties of the internal phase (as discussed in the previous section) influence the final dewetting morphology. The elastic and cohesive nature of the gel phase limits mobility, resulting in structurally arrested films. Overall, the bottom-view imaging reveals that while both systems undergo *n*-heptane evaporation and surfactant deposition, the internal phase composition strongly influences the spatial organization of the residual film.

4 Conclusions

We investigated the dynamic behavior of emulsion-laden drops containing either water or gel as the internal phase, using *n*-heptane with Span 80 micelles as the continuous phase. By analyzing the process in distinct stages of impact, post-impact spreading, and drying/evaporation, we assess how the internal phase state correlates with droplet evolution and final deposition. Within our experimental resolution, the impact dynamics are comparable for water and gel emulsions. For the impact-stage maximum spreading, a unified inertial–capillary–viscous correlation reproduces the measured spreading factors for single-phase liquids and water emulsions, while gel emulsions deviate at higher internal-phase fractions, suggesting additional dissipation not captured by a single effective-viscosity description. Gel emulsions consistently exhibit reduced late-stage spreading compared to water emulsions; this trend is consistent with higher effective dissipation associated with the gelled internal phase and the higher bulk viscosity of gel emulsions. Rheological measurements confirmed shear-thinning behavior in both systems, with gel emulsions showing significantly higher viscosity due to internal phase gelation.

During drying/evaporation, bottom-view imaging shows qualitatively different residue morphologies: water emulsions leave isolated, near-circular deposits, whereas gel emulsions form rugged, interconnected networks, consistent with reduced internal mobility and structural arrest during film breakup. Overall, the combined results suggest that internal rheological transitions can influence macroscopic spreading and deposition outcomes under our conditions. These insights are broadly relevant to fields such as inkjet printing, droplet-based coatings, and soft material processing, where control over the deposit morphology is critical. Future work may explore how the surfactant concentration, ambient humidity, or substrate properties interact with emulsion rheology to further tune final deposition patterns. In particular, it would be valuable to investigate how the rheological properties of the internal gel phase, including complex viscosity, elastic modulus, and potential yield stress, influence droplet impact dynamics.

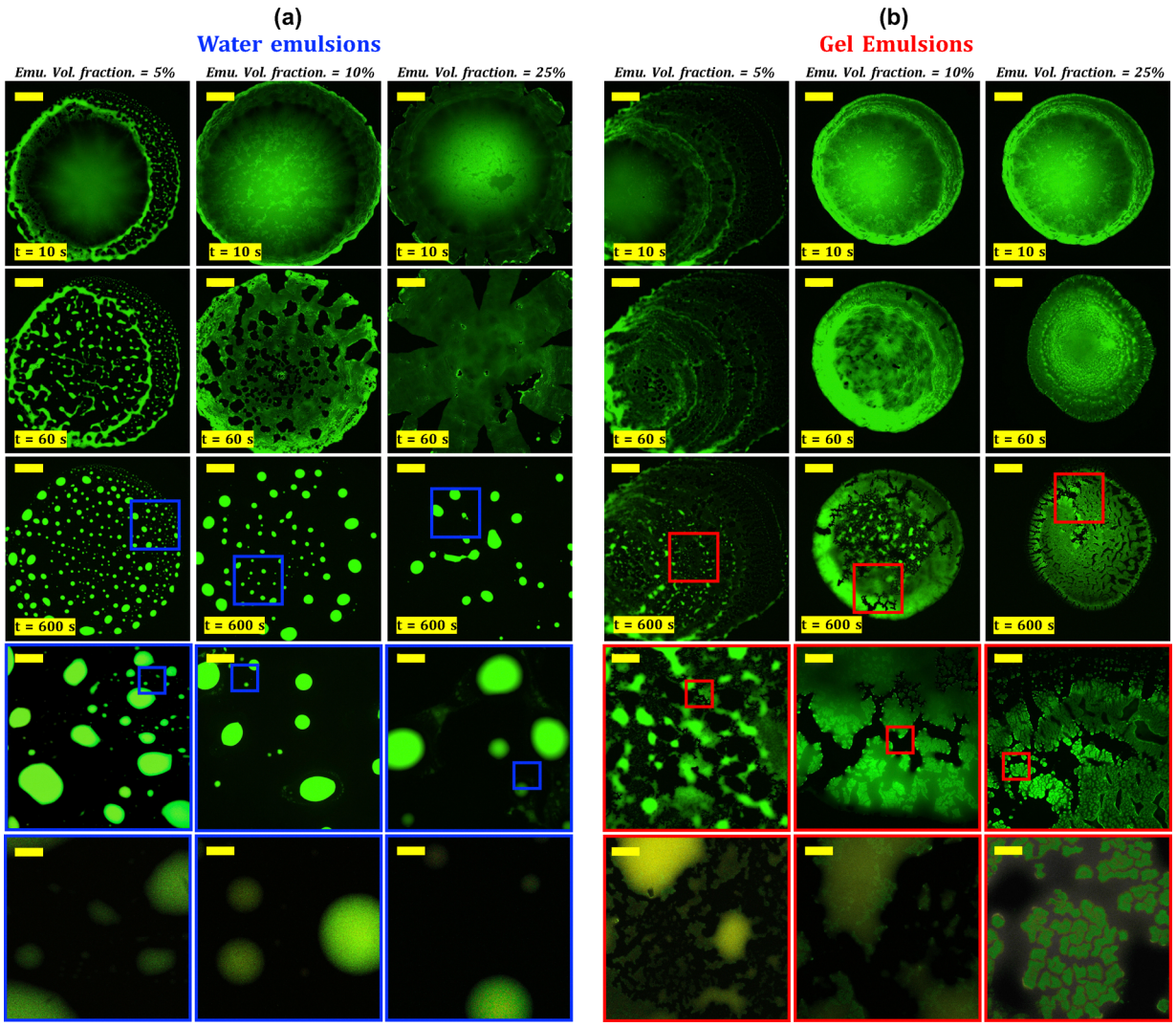

Fig. 5 Bottom-view fluorescence images of drying drops containing (a) water emulsions and (b) gel emulsions in 5, 10, and 25 vol% aqueous phases. Each column corresponds to a different emulsion volume fraction. The top three rows show the temporal evolution of the drying drop at t = 10, 60, and 600 s (from top to bottom). The bottom three rows show increasing magnification of the boxed regions indicated in the third row (t = 600 s), with magnification increasing from top to bottom. As n-heptane evaporates, water emulsions form dispersed, near-circular deposits that become larger and more widely spaced at higher aqueous contents, possibly due to coalescence or water loss. In contrast, gel emulsions form irregular, interconnected structures, consistent with the presence of a more rigid internal phase. Scale bars are 1000 μm for the first three rows and 200 μm and 30 μm for the lower rows (from top to bottom).

Conflicts of interest

There are no conflicts to declare.

Data availability

All data underlying the results are available as part of the article and no additional source data are required.

All experimental procedures and analysis protocols are described in detail within the manuscript and supplementary information (SI). The SI contains additional rheological characterization, supplementary droplet impact experiments, normalized spreading dynamics, contact angle measurements, and tables summarizing the dimensionless numbers used in the analysis. See DOI: https://doi.org/10.1039/d6sm00195e.

Acknowledgements

The authors acknowledge financial support from CONACYT-SENER, managed by the National Council for Science and Technology of Mexico (CONACYT), the Natural Sciences and Engineering Research Council of Canada (NSERC) through a Discovery Grant (RGPIN-2025-05740), and the Department of National Defence (DND)/NSERC Discovery Grant Supplement. Additional support was provided by the University of Calgary's Canada First Research Excellence Fund (CFREF) Program and the Global Research Initiative for Sustainable Low-Carbon

Unconventional Resources. Infrastructure funding from the Canada Foundation for Innovation (CFI) through CFI JELF Project no. 33700 is gratefully acknowledged.

References

1 C. Josserand and S. T. Thoroddsen, Drop impact on a solid surface, *Annu. Rev. Fluid Mech.*, 2016, **48**, 365–391.
2 Y. Yu, H. Zhu, H. E. Ozkan, R. C. Derksen and C. R. Krause, Evaporation and deposition coverage area of droplets containing insecticides and spray additives on hydrophilic, hydrophobic, and crabapple leaf surfaces, *Trans. Am. Soc. Agric. Biol. Eng.*, 2009, **52**(1), 39–49.
3 Y. Yu, J. M. Zhu, H. Frantz, M. E. Reding, K. C. Chan and H. E. Ozkan, Evaporation and coverage area of pesticide droplets on hairy and waxy leaves, *Biosyst. Eng.*, 2009, **104**(3), 324–334.
4 M. Auliano, D. Auliano, M. Fernandino, P. Asinari and C. A. Dorao., Can wicking control droplet cooling?, *Langmuir*, 2019, **35**(20), 6562–6570.
5 W. Qi and P. B. Weisensee, Dynamic wetting and heat transfer during droplet impact on bi-phobic wettability-patterned surfaces, *Phys. Fluids*, 2020, **32**(6), 067110.
6 D. Bonn, J. Eggers, J. Indekeu, J. Meunier and E. Rolley, Wetting and spreading, *Rev. Mod. Phys.*, 2009, **81**(2), 739–805.
7 G. S. Nyashina, K. Yu Vershinina and P. A. Strizhak, Impact of micro-explosive atomization of fuel droplets on relative performance indicators of their combustion, *Fuel Process. Technol.*, 2020, **201**, 106334.
8 B. Han, G. Young Yun, J. William Boley, S. Haidong Kim, J. Young Hwang, G. T.-C. Chiu and K. Park, Dropwise gelation-dehydration kinetics during drop-on-demand printing of hydrogel-based materials, *Int. J. Heat Mass Transfer*, 2016, **97**, 15–25.
9 Z. Jiao, F. Li, L. Xie, X. Liu, B. Chi and W. Yang, Experimental research of drop-on-demand droplet jetting 3d printing with molten polymer, *J. Appl. Polym. Sci.*, 2017, **135**(9), 45933.
10 J. Kettle, T. Lamminmäki and P. Gane, A review of modified surfaces for high speed inkjet coating, *Surf. Coat. Technol.*, 2010, **204**(12), 2103–2109.
11 C. Leuner and J. Dressman, Improving drug solubility for oral delivery using solid dispersions, *Eur. J. Pharm. Biopharm.*, 2000, **50**(1), 47–60.
12 A. Kumar and D. Kumar Mandal, Impact of emulsion drops on a solid surface: The effect of viscosity, *Phys. Fluids*, 2019, **31**(10), 102106.
13 A. Deblais, R. Harich, D. Bonn, A. Colin and H. Kellay, Spreading of an oil-in-water emulsion on a glass plate: phase inversion and pattern formation, *Langmuir*, 2015, **31**(22), 5971–5981.
14 M. Piskunov, A. Semyonova, N. Khomutov, A. Ashikhmin and V. Yanovsky, Effect of rheology and interfacial tension on spreading of emulsion drops impacting a solid surface, *Phys. Fluids*, 2021, **33**(8), 083309.
15 M. Cordova-Gonzalez and S. H. Hejazi, Integrating phase change materials and spontaneous emulsification: In-situ particle formation at oil–water interfaces, *Colloids Surf., A*, 2024, **698**, 134439.
16 V. S. S. Gonçalves, P. Gurikov, J. Poejo, A. A. Matias, S. Heinrich, C. M. M. Duarte and I. Smirnova, Alginate-based hybrid aerogel microparticles for mucosal drug delivery, *Eur. J. Pharm. Biopharm.*, 2016, **107**, 160–170.
17 C. O. Cardoso, R. Ferreira-Nunes, M. Cunha-Filho, T. Gratieri and G. M. Gelfuso, In situ gelling microemulsion for topical ocular delivery of moxifloxacin and betamethasone, *J. Mol. Liq.*, 2022, **360**, 119559.
18 M. Bhat, R. Sakthikumar and D. Sivakumar, Fuel drop impact on heated solid surface in film evaporation regime, *Chem. Eng. Sci.*, 2019, **202**, 95–104.
19 A. Semyonova, N. Khomutov, S. Misyura and M. Piskunov, Dynamic and kinematic characteristics of unsteady motion of a water-in-oil emulsion droplet in collision with a solid heated wall under conditions of convective heat transfer, *Int. Commun. Heat Mass Transfer*, 2022, **137**, 106277.
20 E. Kompinsky, G. Dolan and E. Sher, Experimental study on the dynamics of binary fuel droplet impacts on a heated surface, *Chem. Eng. Sci.*, 2013, **98**, 186–194.
21 M. Aytouna, D. Bartolo, G. Wegdam, D. Bonn and S. Rafaï, Impact dynamics of surfactant laden drops: dynamic surface tension effects, *Exp. Fluids*, 2010, **48**(1), 49–57.
22 S. Mo An and S. Yong Lee, Maximum spreading of a shear-thinning liquid drop impacting on dry solid surfaces, *Exp. Therm. Fluid Sci.*, 2012, **38**, 140–148.
23 E. Jambon-Puillet, O. Carrier, N. Shahidzadeh, D. Brutin, J. Eggers and D. Bonn, Spreading dynamics and contact angle of completely wetting volatile drops, *J. Fluid Mech.*, 2018, **844**, 817–830.
24 M. Cordova-Gonzalez, J. Song, P. Bazazi and S. H. Hejazi, *J. Colloid Interface Sci.*, 2026, **714**, 140170.
25 C. J. Brinker and G. W. Scherer, Sol–gel–glass: I. gelation and gel structure, *J. Non-Cryst. Solids*, 1985, **70**(3), 301–322.
26 E. Katoueizadeh, M. Rasouli and S. Mojtaba Zebarjad, A comprehensive study on the gelation process of silica gels from sodium silicate, *J. Mater. Res. Technol.*, 2020, **9**(5), 10157–10165.
27 A. R. Marsh, III, G. Klein and T. Vermeulen, Polymerization kinetics and equilibria of silicic acid in aqueous systems, *Tech. Rep.*, 1975, 1–184.
28 X. Sun, J. Zhao, T. Chen and X. Liu, Colloidal particle size of fumed silica dispersed in solution and the particle size effect on silica gelation and some electrochemical behaviour in gelled electrolyte, *J. Solid State Electrochem.*, 2016, **20**(3), 657–664.
29 L. T. Pham and D. G. Hatzignatiou, Rheological evaluation of a sodium silicate gel system for water management in mature, naturally-fractured oilfields, *J. Pet. Sci. Eng.*, 2016, **138**, 218–233.
30 F. Gaboriaud, A. Nonat, D. Chaumont and A. Craievich, Structural model of gelation processes of a sodium silicate sol destabilized by calcium ions: combination of saxs and rheological measurements, *J. Non-Cryst. Solids*, 2005, **351**(4), 351–354.

31 A. S. Koneva, E. A. Safonova, P. S. Kondrakhina, M. A. Vovk, A. A. Lezov, Yu. S. Chernyshev and N. A. Smirnova, Effect of water content on structural and phase behavior of water-in-oil (n-decane) microemulsion system stabilized by mixed nonionic surfactants span 80/tween 80, *Colloids Surf., A*, 2017, **518**, 273–282.
32 P. Bazazi and S. Hossein Hejazi, Spontaneous formation of double emulsions at particle-laden interfaces, *J. Colloid Interface Sci.*, 2021, **587**, 510–521.
33 P. Bazazi and S. Hossein Hejazi, Wetting dynamics of nanoparticle dispersions: from fully spreading to non-sticking and the deposition of nanoparticle-laden surface droplets, *ACS Appl. Mater. Interfaces*, 2022, **14**(17), 20280–20290.
34 P. Bazazi, H. A. Stone and S. H. Hejazi, Spongy all-in-liquid materials by in-situ formation of emulsions at oil-water interfaces, *Nat. Commun.*, 2022, **13**(1), 4162.
35 P. Bazazi, H. A. Stone and S. Hossein Hejazi, Dynamics of droplet pinch-off at emulsified oil-water interfaces: Interplay between interfacial viscoelasticity and capillary forces, *Phys. Rev. Lett.*, 2023, **130**(3), 034001.
36 P. Bazazi and H. A. Stone, Pinch-off dynamics of emulsion filaments before and after polymerization of the internal phase, *Soft Matter*, 2025, **21**(7), 1296–1307.
37 L. Peltonen, J. Hirvonen and J. Yliruusi, The behavior of sorbitan surfactants at the water-oil interface: Straight-chained hydrocarbons from pentane to dodecane as an oil phase, *J. Colloid Interface Sci.*, 2001, **240**(1), 272–276.
38 K. Hayashi, T. Shimanouchi, K. Kato, T. Miyazaki, A. Nakamura and H. Umakoshi, Span 80 vesicles have a more fluid, flexible and wet surface than phospholipid liposomes, *Colloids Surf., B*, 2011, **87**(1), 28–35.
39 Y. Ohama, Y. Heike, T. Sugahara, K. Sakata, N. Yoshimura, Y. Hisaeda, M. Hosokawa, S. Takashima and K. Kato, Gene transfection into hela cells by vesicles containing cationic peptide lipid, *Biosci. Biotechnol. Biochem.*, 2005, **69**(8), 1453–1458.
40 D. Bartolo, C. Josserand and D. Bonn., Singular jets and bubbles in drop impact, *Phys. Rev. Lett.*, 2006, **96**(12), 124501.
41 C. Modak, A. Kumar, A. Tripathy and S. Prosenjit, Drop impact printing, *Nat. Commun.*, 2020, **11**(1), 4327.
42 S. Moghtadernejad, C. Lee and M. Jadidi, An introduction of droplet impact dynamics to engineering students, *Fluids*, 2020, **5**(3), 107.
43 B. Gorin, G. Di Mauro, D. Bonn and H. Kellay, Universal aspects of droplet spreading dynamics in newtonian and non-newtonian fluids, *Langmuir*, 2022, **38**(8), 2608–2613.
44 J. M. Gordillo, G. Riboux and E. S. Quintero, A theory on the spreading of impacting droplets, *J. Fluid Mech.*, 2019, **866**, 298–315.
45 S. Chandra, M. di Marzo, Y. M. Qiao and P. Tartarini, Effect of liquid-solid contact angle on droplet evaporation, *Fire Safety J.*, 1996, **27**(2), 141–158.
46 M. Shu, L. Fan, J. Zhang and J. Li, Research progress of water-in-oil emulsion gelated with internal aqueous phase: gel factors, gel mechanism, application fields, and future direction of development, *Crit. Rev. Food Sci. Nutr.*, 2024, **64**(17), 6055–6072.
47 G. Sun, C. Li, F. Yang, B. Yao and Z. Xiao, Experimental investigation on the gelation process and gel structure of water-in-waxy crude oil emulsion, *Energy Fuels*, 2017, **31**(1), 271–278.
48 R. Araujo Mantovani, A. Luiz Fazani Cavallieri and R. Lopes Cunha, Gelation of oil-in-water emulsions stabilized by whey protein, *J. Food Eng.*, 2016, **175**, 108–116.
49 L. Liu, G. Cai, W. Wang, B. He and P. Amy Tsai, On the maximum spreading of viscous droplets impacting flat solid surfaces, *J. Fluid Mech.*, 2025, **1018**, A42.
50 N. Laan, K. G. de Bruin, D. Bartolo, C. Josserand and D. Bonn, Maximum diameter of impacting liquid droplets, *Phys. Rev. Appl.*, 2014, **2**(4), 044018.
51 V. Sanjay and D. Lohse, Unifying theory of scaling in drop impact: Forces and maximum spreading diameter, *Phys. Rev. Lett.*, 2025, **134**(10), 104003.
52 P. Shah and M. M. Driscoll, Drop impact dynamics of complex fluids: a review, *Soft Matter*, 2024, **20**, 4839–4858.
53 M. Nicolas, Spreading of a drop of neutrally buoyant suspension, *J. Fluid Mech.*, 2005, **545**, 271–280.
54 V. Grishaev, C. S. Iorio, F. Dubois and A. Amirfazli, Complex drop impact morphology, *Langmuir*, 2015, **31**, 9833–9844.
55 F. Boyer, E. Sandoval-Nava, J. H. Snoeijer, J. F. Dijksman and D. Lohse, Drop impact of shear thickening liquids, *Phys. Rev. Fluids*, 2016, **1**, 013901.